Signature of gravity wave propagations from the Troposphere to Ionosphere

Hisao Takahashi[1], Cosme A. O. B. Figueiredo[1], Patrick Essien[2], Cristiano M. Wrasse[1], Diego Barros[1], Prosper K. Nyassor[1], Igo Paulino[3], Fabio Egito[3], Geangelo M. Rosa[4], Antonio H. R. Sampaio[4]

1. Space Weather Division, Instituto Nacional de Pesquisas Espaciais, São José dos Campos, Brazil

2. University of Cape Coast, Department of Physics, Cape Coast, Ghana

3. Unidade acadêmica de Física, Universidade Federal de Campina Grande, Campina Grande, Brazil

4. Federal Institute for Education, Science and Technology Baiano (IF Baiano), Bom Jesus da Lapa, Brazil

10 *Correspondence to*: Hisao Takahashi (hisao.takahashi@inpe.br)

Abstract. We observed a gravity wave (GW) signature in the OH emission layer in the upper mesosphere, and 4 hours later, a medium-scale traveling ionospheric disturbance (MSTID) in the OI 630 nm emission layer. Spectral analysis of the two waves did show that both have almost the same wave characteristics: wavelength, period, phase speed and propagation direction, respectively, 200 km, 60 min, 50 m/s, propagating toward the Southeast. ~~During the MSTID occurrence, concentric~~

15 ~~wavefronts were also observed in the ionosphere by detrended total electron content (dTEC) maps~~. From the gravity wave ray-tracing simulation for the mesospheric gravity wave, we found that the wave came from a tropospheric deep convection spot and propagated up to the 140 km altitude. Regarding the same wave characteristics between mesospheric GW and MSTID, two possible cases are investigated: a direct influence of the GW oscillation in the OI 630 nm emission height and the generation of a secondary wave during the GW breaking process. The concentric wave structure suggests the generation of a

20 secondary wave after the primary wave was dissipated in the lower thermosphere. This is the first time to report an observational event of gravity wave propagation from the troposphere, mesosphere to thermosphere-ionosphere in the south American region.

1. Introduction

25 A deep cloud convection in the troposphere generates vertical (up and down) air-mass movement launching a variety of gravity waves into the stratosphere. Atmospheric gravity waves (GWs) have important roles in transporting the energy and momentum from the lower to upper atmosphere and ionosphere. A part of energy and momentum is deposited in the mesosphere lower-thermosphere (MLT) region through wave breaking and altering the background wind field. Some of the GWs produce secondary waves and propagate further upwards into the thermosphere where it modulates ionospheric plasma (Hocke and

30 Schlegel,1996, Nicolls et al., 2014). A part of Medium-Scale Travelling Ionospheric Disturbances (MSTIDs) has its origin in

the passage of gravity waves in the ionosphere (Otsuka, 2018). Observations of GW propagation in the thermosphere have been carried out by many researchers since Hines (1960) has presented theoretical background for the GW propagation in the ionosphere. Rottger (1973) suggested the role of GWs in the ionospheric irregularities.

GW observations in the mesosphere have been carried out by measuring short period temporal variation of the mesospheric airglow (Hydroxyl and atomic oxygen OI 557.7 nm emissions) by airglow photometers in 1970-1990 (e. g., Takahashi et al, 1999). After 1990 airglow digital imagers were used to monitor GWs in two-dimensional forms (e.g., Taylor et al. 2009, Dare-Idowu et al. 2020, Nyassor et al., 2021). Dynamical processes in the mesosphere to thermosphere were studied by OH and oxygen 630.0 nm airglow imaging by Kubota et al. (2000), Taori et al. (2013) and most recent by Ramkumar et al. (2021). In case of GWs in the stratosphere, satellite-onboard GPS radio occultation measurements have made it possible to observe GWs by vertical profile of the temperature variability on a global scale (Tsuda, 2014, Xu et al., 2017).

There are many previous works on the GW propagations in the stratosphere, mesosphere and ionosphere individually. However, it has been difficult to monitor an event of GW propagating through the troposphere up to the ionosphere. Smith et al. [2013] observed GW waves in the OH and OI 557.7 nm emission layers in the mesosphere to lower thermosphere (MLT) region (85-100 km) and OI 630.0 nm emission layer (around 240 km altitude) in the thermosphere and discussed on the mountain waves from the mesosphere to ionosphere. They attributed the wave structure in the ionosphere as due to secondary waves. Azeem et al. (2015), for the first time, reported the occurrence of circular GW structures in the stratosphere, mesosphere and ionosphere during a tropospheric convective storm. They observed concentric wave structures in the stratosphere by the Atmospheric Infrared Sounder(AIRS) onboard Aqua satellite (https://airs.jpl.nasa.gov/), and by an optical imaging radiometer (VIIRS) onboard Suomi satellite (https://www.nasa.gov/mission_pages/NPP/main/index.html), and in the ionosphere by ground-based GPS receivers. Prior to this work, Nishioka et al. (2013) has reported concentric gravity waves in the ionosphere which were induced by a severe convective system (supercell) in the troposphere. The concentric waves lasted for more than 7 hours. Nyassor et al. (2021) reported the first mesospheric concentric gravity waves excited by thunderstorm. Takahashi et al. (2020) presented the generation and propagation of MLT-GWs and concentric MSTIDs in the ionosphere during a deep convection activity in the troposphere over the south American continent.

Regarding propagation of GWs from the lower to upper atmosphere, Vadas (2007), as the first time, studied propagation property of GWs from the troposphere to the thermosphere for the horizontal wavelength of 10 to 1000 km and the period of 10 to 100 min. The author presented the GW dissipation altitudes depending on their horizontal wavelength and period. In case of the horizontal wavelength of 200 km and its period of 60 min, for example, the model predicts dissipation above 120 km altitude. It means that the dissipation produces a body force and generates secondary waves.

There is a difficulty to observe a gravity wave from its origin (source) in the troposphere following up to the thermosphere. During the upward propagation, it could change its wave characteristics under the background atmosphere condition, dissipating and producing secondary waves changing the horizontal wavelength, phase speed and propagation direction (Vadas

and Crowley, 2010). It would take several hours to reach from the troposphere to the mesosphere-lower thermosphere (Vadas and Liu, 2013), which makes it difficult to follow the wave step by step. Recent observation of concentric wavefronts in the
65 stratosphere, mesosphere and thermosphere (Azeem et al, 2015) would be rather a rare case. Further observational evidence would be necessary to clarify the propagation processes. The purpose of the present work is to report a case of gravity wave propagation directly from Tropospheric convection to the mesosphere and thermosphere/ionosphere. For investigating the propagation of gravity waves, data from airglow OH imager in the mesosphere and OI 630 nm imager from the thermosphere/ionosphere, ionosondes ~~and a GNSS receiver network~~ are used.

70 **2. Observations**

Airglow observation has been carried out at Bom Jesus da Lapa (hereafter BJL), 13.3° S, 43.5° W, geomag.14.1° S, since 2019. The observation site is located under the equatorial ionospheric anomaly (EIA) belt. Equatorial plasma bubbles can also be frequently observed. An all-sky airglow imager equipped with 3-inch optical interference filters (for 630.0 nm, 557.7 nm and OH-NIR(710-930 nm) takes 180° wide images with a time sequence of ~ 5 min. Exposure time for each filter is 15 s for
75 the OH-NIR and 90 s for the OI 630.0 nm and 557.7 nm images. The imager characteristics have been presented by Wrasse et al. (2021). In the present study we used the image data from December 2019 to September 2020. During this period, we selected 13 days of observation to analyze wave structures in the OI 630 nm images.

~~Ionospheric Total Electron Content (TEC) maps are produced by using ground-based GNSS receiver network over the South America (Takahashi et al., 2016). The TEC maps over South America with 10 min intervals are available at EMBRACE's~~
80 ~~website (http://www2.inpe.br/climaespacial/portal/en/). To retrieve small amplitude of TEC variability, less than 1.0 TEC unit of spatial variation, we plot the vertical TEC time series from the individual receiver, and to pick up a fraction from running means as follows,~~

~~dTEC (t) = TEC(t) – <TEC(t +/- 30 min)>~~
~~where the symbol < > means the time average between the +/- 30 min interval. The temporal resolution of the dTEC map is~~
85 ~~one min. The spatial resolution is a square of 0.25° x 0.25°, then taking a running average with 5 points. The dTEC(t), therefore, can be plotted on the map with 1.25° square (~130x130 km) by one min time interval. Any wave propagation mode, of which oscillation amplitude being less than one TECu and the temporal oscillation between 5 and 30 min can be plotted (Figueiredo et al. 2018, Essien et al. 2021).~~

In the present work, the data from the ionosondes were used to observe the vertical drift of the F-layer and to calculate the
90 electron density profile. Three digital ionosondes (DPS-4) (http://www.digisonde.com/instrument-description.html) have been operated one at São Luís (2.6° S, 44.2° W, geomag. 3.9°S), Fortaleza (3.9° S, 38.4° W, geomag. 6° S), and Cachoeira Paulista (22.7° S, 45.0° W, geomag. 18.1° S). The DPS-4 sounder has a 500 W peak power, covering a frequency range from 0.5 to 30 MHz. Ionograms are taken with a time interval of 10 minutes.

3 Results

95 ### 3.1 OH images

On the night of 18-19 January 2020, around 22:30 to 23:30 UT (19:30-20:30 Local Time), the airglow OH images showed two wave structures passed over BJL. Figure 1 shows the OH images at the moment of one of the wavefronts passing over the zenith. The images are projected on the geographic coordinates. The horizontal extension of the image is approximately 500 km and the blue dot indicates the location of the BJL observation site. In Figure 1(a), there are two wave structures, one is

100 shorter wavelength in the northwest side of the image (top left side) (GW-1) and another is a longer wavelength, one wavefront over the zenith (blue dot) and the other at the SE, indicated by the blue arrows (GW-2). Three sequential images with a time interval of 10 minutes indicate that the wavefront is moving toward the SE (indicated by a red arrow in Fig 1(b)). The propagation mode can be clearly seen if keograms are made by using the meridional and longitudinal cuts as a function of time. Figure 2 shows the keograms (zonal and meridional cuts) between 22:30 and 28:30 (04:30) UT. Looking at the GW-2,

105 two bright bands propagating from the North to South and the West to East can be seen. The broad bright band passing over the zenith from the NE to SW through the night is the Galactic Milky way.

110

Fig. 1. Geographically coordinated OH images observed at Bom Jesus da Lapa (BJL), 13.3° S, 43.5° W, geomag.14.1° S, at 23:30 UT (left), 23:41 UT (center) and 23:51 UT (right) on the night of 18-19 January 2020. Blue dots indicate the zenith of BJL. The blue arrows indicate the wave fronts of the longer wavelength one (GW-2). The red-arrow indicates the direction of propagation.

115
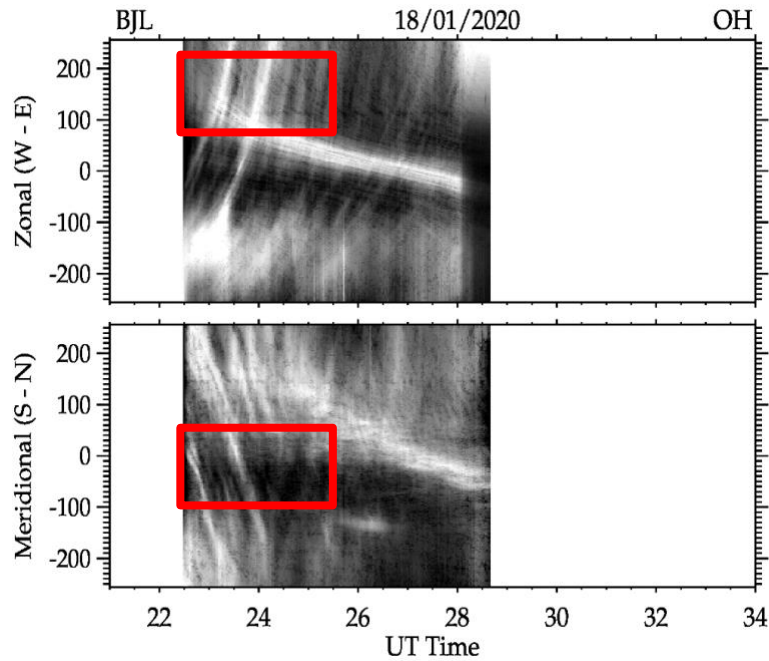
Fig. 2. Keograms of OH images observed at BJL in the night of 18-19 January 2020. Meridian cuts along the W-E direction (upper panel) and the S-N direction (lower panel) are shown as a function of time from 22:00 to 30:00 (06:00) UT. The red color rectangular boxes are where the FFT spectral analysis were taken.

120

For calculating the wave characteristics (horizontal wavelength, period, phase velocity), we used Fast Fourier Transform (FFT) spectral analysis (Wrasse et al., 2007, Figueiredo et al., 2018, Essien et al., 2018). Image samples used in the calculation are indicated by red boxes in Figure 2. The wave characteristics of the longer wave (GW-2) are, the horizontal wavelength of 217.9±12 km, the period of 60.6±03 min, the phase speed of 59.9±5 m/s, and the propagation direction of 148.5± 10°. For the

125 short wave (GW-1) the wave characteristics was also obtained: the horizontal wavelength of 36.2±1 km, the period of 15.8±0.8 min, the phase speed of 38.3±2 m/s, and the propagation direction of 135.0±10°.

3.2 OI 630 nm image

Figure 3 presents 3 sequential images of the OI 630 nm emission between 03:20 UT and 03:48 UT. The top 3 panels are original images, and the bottom 3 panels are the residual images which are subtracted from the one hour averaged image. From

130 the residual images one can see two dark bands in the southwest of BJL propagating toward East, which seem to be the Medium Scale Travelling Ionospheric Disturbance, named as MSTID-1. We checked any contamination of the OH emission in the OI

630 nm image. No such wavelike structure could be observed in the OH images during the same period. The bright OI 630 emission intensity over the northwest part of the sky should be the midnight downward drift of the F-layer accompanied by the Midnight Temperature Maximum (MTM) in the thermosphere (Colerico et al.,1996, Figueiredo et al., 2017). One can also

135   notice the presence of the equatorial plasma bubbles (EPBs) (at least two depletions) in the northwest of BJL, which are also drifting toward the East. The difference between the EPBs and MSTID-1 is clear to see. The EPBs are extending from the equator side and the MSTID is elongating from the South. During the 28 min of the time interval (from Figure 3(a) to (c), a dark band moved toward the East by ~90 km. In order to get the wave characteristics of MSTID-1 from the OI 630 images, we used the FFT spectral analysis for the OI 630 keogram (not shown here), which is similar to the OH image analysis

140   mentioned above (Wrasse et al, 2007). The results are the horizontal wavelength of 201.7±13 km, the period of 64.2 ± 33 min, the phase speed of 52.4 ± 27m/s and the propagation direction of 113.2 ±10°. The characteristics of the wave propagation in the OH emission layer and OI 630 nm emission layer are summarized in Table 1. The movement of wave fronts of MSTID-1 is presented in the supporting file: [OI 6300_movie.mp4].
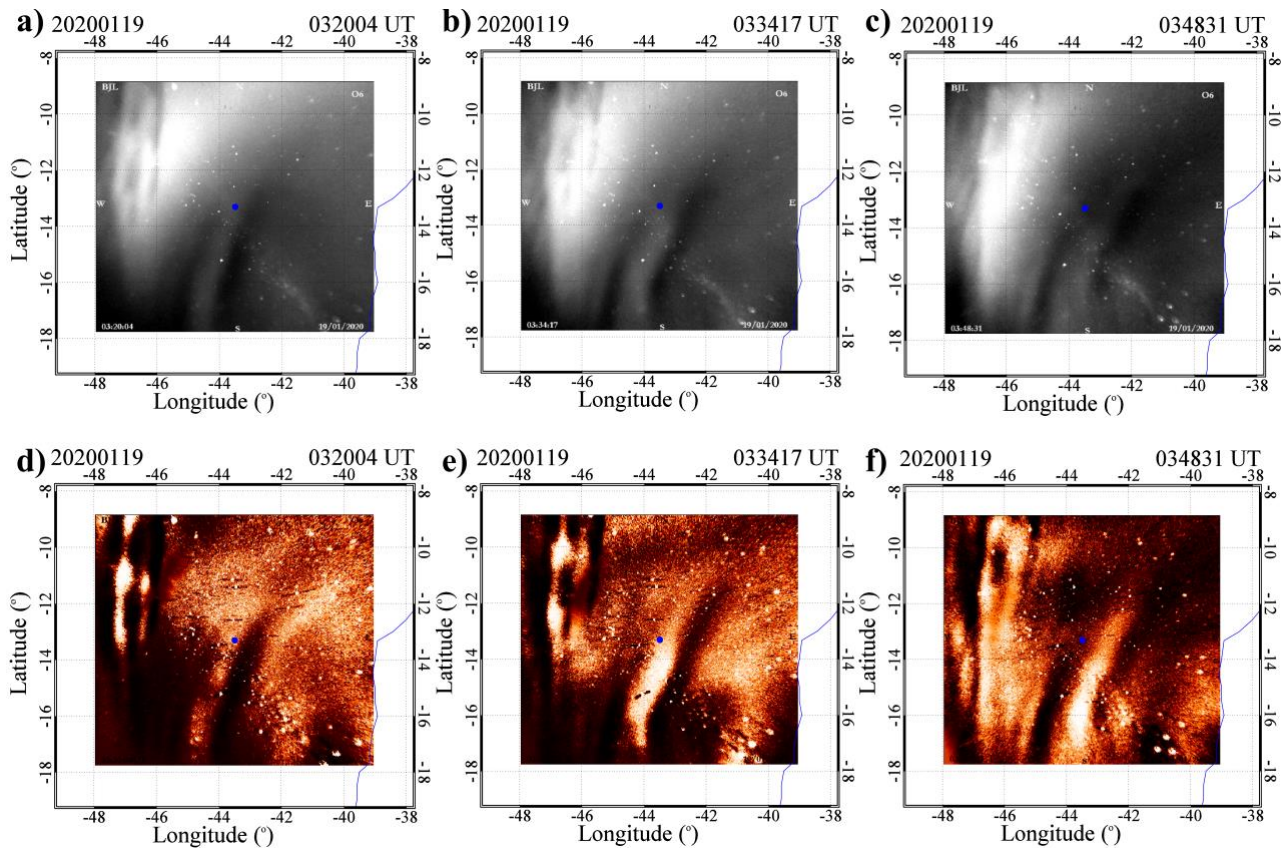
145

Fig. 3. Geographically coordinated OI 630 nm images observed at Bom Jesus da Lapa (BJL) at 03:20 UT (left), 03:34 UT(center) and 03:48 UT (right) on the night of 18-19 January 2020. The top 3 images are original and the bottom 3 images

are residual subtracted from the one hour averaged image. Blue dots indicate the location of BJL. MSTID-1 (lower/middle),
EPBs (upper left corner) and MTM (upper left) can be seen (see Text).

150

Table 1. *Wave Characteristics obtained by the OH images in the MLT region (GW-1 and GW-2), and OI 630 nm images in the thermosphere (MSTID-1) and dTEC maps in the ionosphere (MSTID-2). (The values in parentheses are the error range.)*

155

GWs & MSTIDs	OH (22-00 UT) (GW-1)	OH (23-00 UT) (GW-2)	OI630 (03-04 UT) (MSTID-1)	dTEC (02-04 UT) (MSTID-2)
λ_H (horiz wave length) (km)	36.2 (1.0)	217.9 (12.3)	201.7 (13.4)	360 (50)
τ (period) (min)	15.8 (0.8)	60.6 (3.0)	64.2 (33.2)	26.5 (2)
Vp (phase speed) (m/s)	38.3 (2.0)	59.9 (4.5)	52.4 (26.9)	226 (20)
Az (Azimuth) (deg)	135.0 (10.0)	148.5 (10.0)	113.2 (10.0)	Circular

3.3 dTEC map

A small amplitude of perturbation of the ionospheric total electron content (TEC) was retrieved from the dTEC analysis mentioned in the previous section. Figure 4 depicts a snapshot of the dTEC map at 03:44 UT (00:44 LT) on 18-19 January 2020. The red squares indicate where the TEC disturbance was larger than 0.2 TECu from the running average level. The spatial resolution of the map, in this case, is around 130 km, and the temporal resolution is 1 min. From previous works (Figueiredo et al., 2018, Essien et al., 2021), it is known that the amplitude of oscillation of TEC during the passage of MSTIDs is between 0.1 to 0.2 TECu. Our present results, the dTEC variation of -0.4 to +0.2 TEC are similar to the previous works.

165
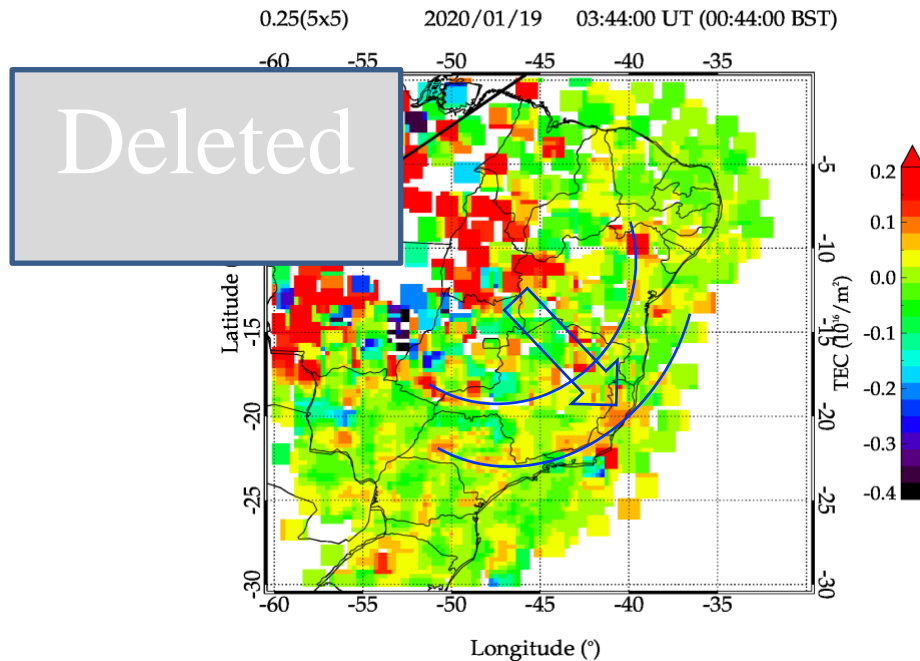
0.25(5x5)   2020/01/19   03:44:00 UT (00:44:00 BST)

Fig. 4 dTEC Map in the equatorial and low latitude of Brazil, taken at 03:44 UT (00:44 LT at 45°W), 18-19 January 2020. The black line indicates the geomagnetic equator, and the blue circumferences indicate wave crests of the MSTID. The top/left corner "0.25(5x5)" indicates a spatial resolution of the map as 1.25°x 1.25°(~130 x 130 km).

170

The accumulated red squares at around (5-12° S, 45-55° W) in Figure 4 indicate a region where the ionosphere is disturbed, most probably due to the EPBs seen in the OI 630 nm images in Figure 3. One can further notice that there is an increase of disturbance (the color of yellow to red squares) on the circumferences indicated by light blue lines, from the East to South region of the map, which is identified as a MSTID 2. The center of the circumferences falls on (12° S, 47° W). Since the wave fronts are curved, it is a concentric wave. The partial concentric form should be caused by the EPB activity in the NW side of the (12° S, 47° W) region where the TEC depletions were going on. It also might be due to the wind filtering effect by the background wind field as reported by Nishioka et al. (2013). From the distance between the wave fronts, the horizontal wavelength was estimated to be 360 ± 50 km. To obtain the wave characteristics, the keogram analysis was also applied. Longitudinally (latitudinally) sliced dTEC map at 13.0° S (43.0° W) as a function of time is shown in Figure 5. During the time interval of 02:30 to 04:00 UT in the 10 to 15° S region (highlighted by the rectangular boxes) one can notice a periodic structure of dTEC perturbation in both longitudinal and latitudinal cuts (indicating by the blue dashed lines), suggesting a passage of disturbance, named as MSTID 2. The disturbance appeared around 01:30 to 04:00 UT in the 47° to 55° W longitudes; it was due to the equatorial plasma bubbles. Although the spatial resolution of the keogram image is not enough to

~~estimate the horizontal wavelength, the periodicity could be obtained, which is 26.5 ± 2.0 min. The phase velocity is, therefore~~

185   ~~calculated to be 226 ±15 m/s. The wave characteristics of the MSTID-2 are also summarized in Table 1.~~
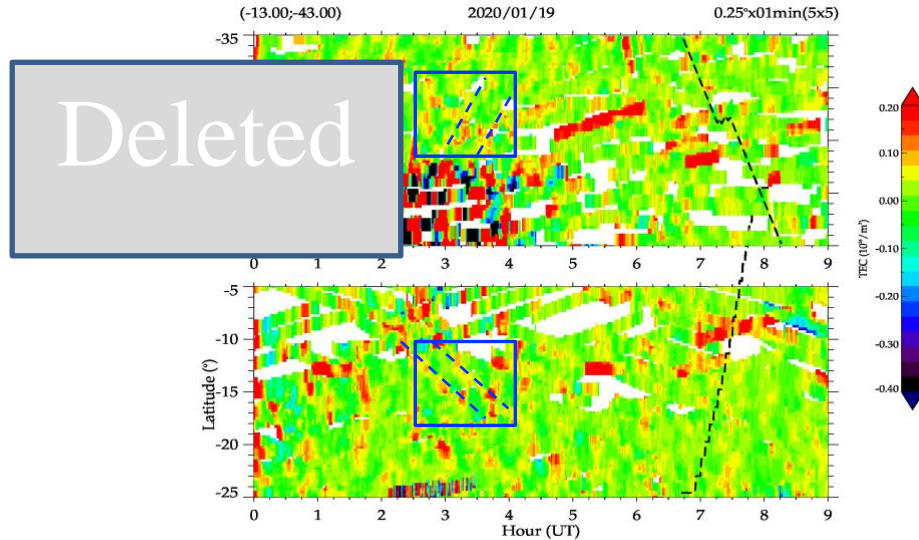
190

4 Discussion

Through the evening to midnight over the Bom Jesus da Lapa (BJL) airglow observation site (17° S, 38° W) on 18-19 January 2020, we observed a relatively long wavelength and slow speed GW (GW-2) in the OH emission layer (~87 km altitude) at around 23:00 UT. In 4 hours later (03:00 UT), we observed a wave structure in the OI 630 nm emission layer in the lower

195   ionosphere (~240 km altitude) (MSTID-1). The two different waves, one from MLT and the other from the thermosphere, had almost the same wave characteristics, i. e, a same horizontal wavelength (210 ± 10 km), same period (62 ± 5 min) and the same phase speed (55 ± 5 m/s). The propagation directions of the two emissions, however, are slightly different, OH showing 149° against OI 630 being 113°, the difference of 36°. The OH wavefronts are extended longer than 500 km. On the other hand, the OI 630 wave was limited in the southern sky with a relatively short duration (~60 min). Such coincident occurrence

200   of the wave structure called our attention to further investigate whether these waves have the same origin from the lower atmosphere, *i. e.,* both are primary waves, or one of the waves in the thermosphere was due to the secondary wave generated in the lower atmosphere.

4.1 GW Ray-Tracing and Tropospheric Convection Origin

For studying the wave propagation, we used a wave ray-tracing method (Paulino et al. 2013, Vadas et al., 2019, Nyassor et al.,
205 2021) to find out the source of the waves in the lower atmosphere. The wind model used in this work was according to the

NRLMSISE-00 (Picone et al., 2002) and Horizontal Wind Model (HWM14) (Drob et al., 2015). Figure 6 presents the Ray-

Tracing trajectories of the GW-2 for the case of no-wind and with-wind model.
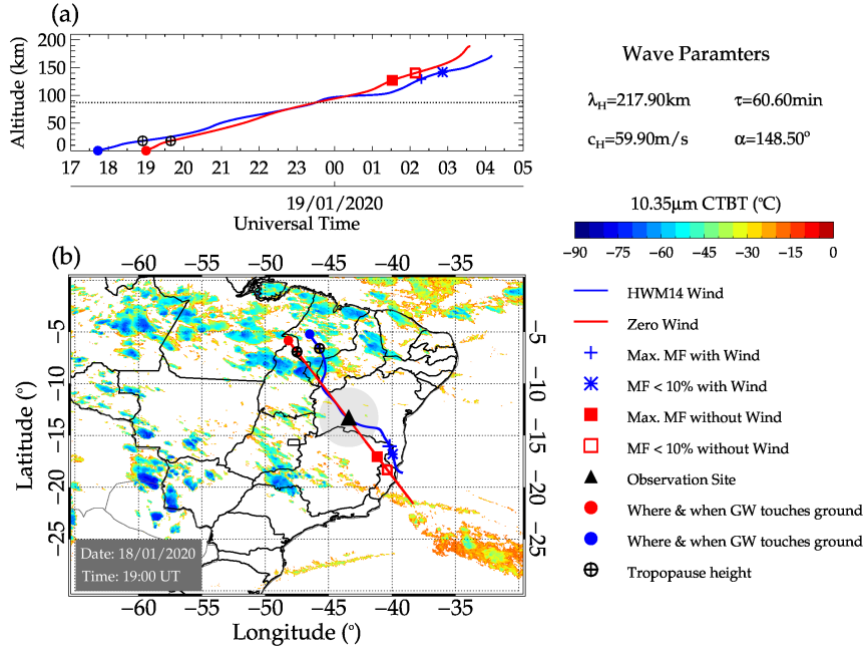
Fig. 6. Ray tracing (backward and forward) of the observed gravity wave (λ_h=217.9 km) starting at 87 km altitude at BJL on
210 the night of 18 January 2020 at 23:00 UT. The vertical trajectory versus time (top) and horizontal distance (bottom) are shown.
The red line is of the case of no-wind and the blue line is of the with-wind model. The blue triangle is the starting point of the
ray tracing. The background map is the cloud top temperature from NOAA GOES 16 meteorological satellite data (10.35 μ)
on 18 January 2020 at 19:00 UT.

215 The simulation started from 87 km altitude at 23:30 UT and went down (backward tracing) to the ground level at around 19:00
UT, crossing the tropopause (~15 km) at around (7.0° S, 46.5° W) at 19:30 UT. There is a difference of around 200 km of the
tropopause crossing positions between the no-wind and with-wind trajectories, which can be assumed to be an error range in
the present study. Then, we search for any convective system in this region. Figure 6 also shows the cloud top temperature
map produced by GOES-16 (10.35 μ radiation map) at 19:00 UT (https://www.cptec.inpe.br/). It can be seen the convection
220 system spread over the tropical zone 0 -10°S. It is the Intertropical Convergence Zone (ITCZ). One can notice that there is the
lowest temperature spot (-80°C) at (8.5° S, 46.5° W), where a deep convection was in progress. One can notice that this

convection spot is located very close (in an error range of 200 km) to the GW-2 trajectory at the tropopause height. According to the GOES-16 maps, this convection spot started at around 18:00 UT, developing into a much larger area from 19:00 to 23:00 UT and decreasing the intensity after 00:00 UT. During the 5 hours of activity, the convection spot should generate up and down streams inside of the convection cell producing a variety of GWs. The present Ray-Tracing suggests that the observed gravity wave in the OH emission layer started from this convection spot propagating up to the lower thermosphere.

4.2 GW breaking in the thermosphere and generation of a secondary wave

The forward Ray-Tracing shown in Figure 6, on the other hand, went up to 130 km with the momentum flux in the maximum and then it lost the amplitude of oscillation at around 140 km, indicating dissipation of the wave energy. The wave dissipation occurred at the location of (18° S, 40° W) where we observed the wave structure in the OI 630 nm image starting at around 03:00 UT. According to Vadas and Crowly (2010), GW dissipation produces a body force and generates secondary waves. The secondary waves have a variety of wave characteristics. In our present case, we understand that the primary wave observed at the MLT region dissipates in the lower thermosphere, then a secondary wave reaches at the OI 630 emission height, which is located at around 240 km altitude. If this is the case of what happened, the secondary wave had the same characteristic as the primary wave. Vadas and Becker (2018) have discussed in the small- and large-scale secondary waves. According to them, there will be two kinds of secondary waves, one is small scale waves (short horizontal wavelengths) that will be produced during the primary wave breaking process, and the other one is the much longer wavelength (thousands of km) which are produced by a body force generated after the primary GW dissipation. The latter is dependent on the spatial scale of the body force. Bossert et a. (2017), for example, observed secondary waves near the primary (mountain) wave breaking area and found that the horizontal wavelengths are shorter than the primary waves. Smith et al. (2013) reported nearly simultaneous observation of mesospheric GWs by OH airglow and thermospheric GWs by OI 630 nm images. According to their observation, the horizontal wavelength of the OH wave against the OI 630 nm wave is 106 km vs. 255 km, the phase speed of 49.5 m/s vs. 104 m/s, and the period of 36.5 min vs. 42.7 min. Our present case (relatively short wavelength and low phase speed) could be the first case, i.e., secondary wave generated during the primary wave breaking process.

4.3 Possible direct influence of primary wave in the ionosphere

The other possibility of the presence of GWs is a direct influence of the primary wave in the OI 630 nm emission layer. The Ray-Tracing simulation for the MLT GWs did show its dissipation at around 140 km (Figure 6). According to Vadas (2007), the signature of GWs in the thermosphere could be observable even at one or two local density scale heights (15-20 km at around 150 km altitude) above the dissipation altitude. If this is the case, the influence of the primary wave could reach at least at the altitude of 170-180 km where the F-layer bottom side is located. It is worth to check, therefore, the OI 630 nm emission height over BJL during the GW occurrence (03:00-04:00 UT).

The airglow OI 630 nm emission is produced by the dissociative recombination process in the ionosphere:

$O_2^+ + e \rightarrow O(^1D) + O\,(^3P, \,^1S)$
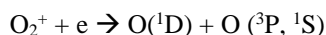
where O(^{1}D) is an excited state of atomic oxygen responsible to emit a photon of 630,0 nm. The emission rate, therefore,
depends on the concentration of the electron density [e] and its height profile (Chiang et al., 2018). The electron density
profile, especially its bottom side profile, could be estimated by ionograms. Unfortunately, there is no ionosonde at BJL.
During the passage of the waves at around 03:00 - 03:30 UT (00:00 - 00:30 LT), two DPS ionosondes, one at Fortaleza (7° S,
38° W), the North of BJL, and the other at Cachoeira Paulista (22.7° S, 45.0° W), the South of BJL, were in a routine
observation mode. The Fortaleza ionogram showed the F-layer peak height (hmF2) at 220±10 km. It is a mean altitude during
the period of 03:00 and 03:20 UT when the ionogram was free from the Spread F. It is very low altitude, due to the Midnight
Collapse of the Ionosphere (Gong et al., 2012). On the other hand, the ionosonde at Cachoeira Paulista observed the peak at
260±10 km. From the estimated electron density profiles, we calculated the OI 630 nm volume emission rates based on the
equation presented by Chiang et al. (2018). The peak emission altitude at Fortaleza was at 200 km. On the other hand, at
Cachoeira Paulista it was at 240 km. The peak altitude at Fortaleza is 40 km lower than Cachoeira Paulista. The BJL site is
located between the two ionosonde sites. Therefore, we assume that the OI 630 nm emission peak altitude at BJL might be
between 200 and 240 km. In this case, a possibility of that the bottom side of the OI 630 nm emission layer would be disturbed
by the primary wave cannot be ruled out. The difference of the propagation direction of 36° between the OH and OI 630 nm
wave fronts could be due to the different wind fields between the two emission altitudes.

4.4 GWs observed by dTECmap

As shown in Figure 4, we could see a concentric wave structure in the dTEC map. The center of the circular waves is located
at around (12.0° S, 47.0° W), which is about the 4.0° South of the convection spot. If one compares the wave characteristics
obtained by the dTEC maps (MSTID-2) and the 630 nm images (MSTID-1), the horizontal wavelength of the former is much
longer (360 km) and the period is shorter (26.5 min). It means that the phase speed of the former is much faster (226 m/s).
Although the characteristics of the two waves are different, they seem to have a same origin. During the period of 19:00 to
23:00 UT, the ITCZ convection spot developed quickly forming a cluster of convection at around (8.0° S, 46.0° W). It could
be possible that these convection spots launched a variety of GW spectra. In order to simulate the wave propagation path of
the circular fronts, the backward Ray Tracing was also applied for one of the concentric waves. The wavefront location and
its altitude were assumed to be at (17.0° S, 43.0° W) and 300 km altitude, respectively, and started from 03:40 UT. The
simulated backward trajectory is shown in Figure 7, where one can see the trajectory went down toward the Northwest
and reached the minimum height at around 100 km altitude at (12.5° S, 48.0° W). It means that this concentric wave did not
come from the lower atmosphere but was generated above 100 km. Vadas and Azeem (2020) presented (see Figure 21 of
Vadas and Azeem (2020)) the backward ray tracing of the GWs from 300 km altitude for the waves with the different
phase speeds, and found that GWs with a phase speeds faster than 200 m/s could not propagate below ~100 km altitude. Our
present case is similar to them. The horizontal distance between the wavefront and the location of the minimum height (at 100
km altitude) is approximately 805 km. This location almost coincided with the center of the concentric waves. These facts and
the GW propagation simulation suggest that the concentric waves started above the mesopause and propagated upwards. It

indicates that they are not primary waves from the troposphere, but a secondary gravity wave generated in the lower thermosphere.
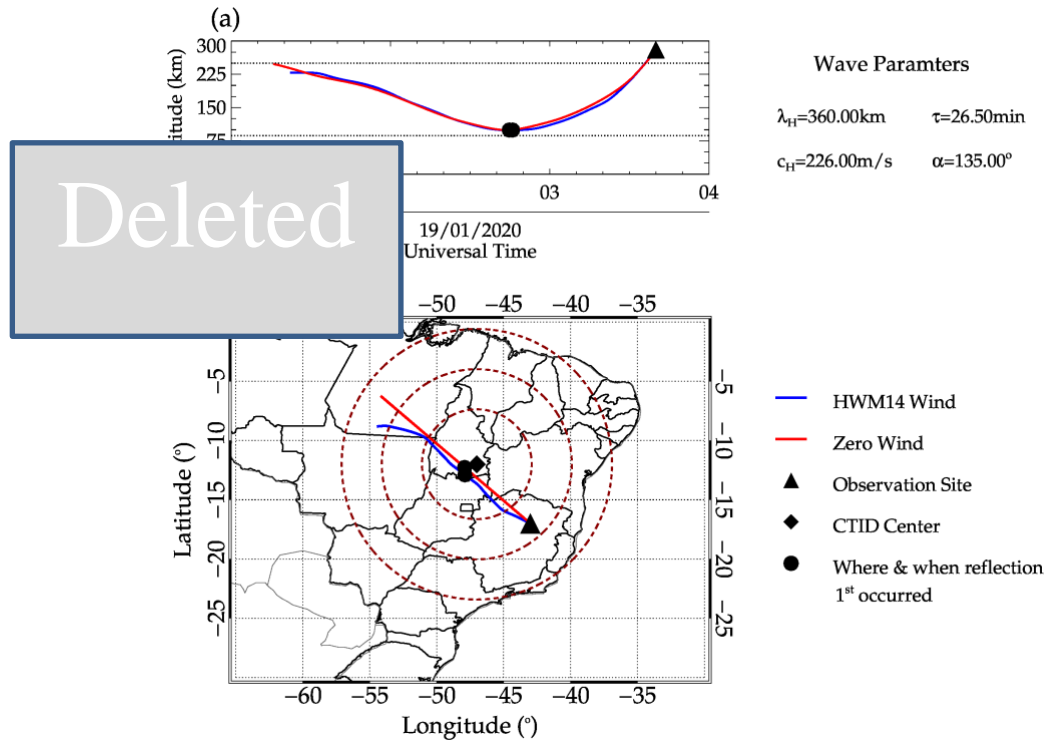
290

Fig. 7. Backward Ray Tracing of the MSTID circular waves, starting from 300 km altitude at (17.0°S, 43.0°W) at 03:40 UT. The vertical trajectory versus time (top) and horizontal distance (bottom) are shown. The red line is in the case of the no-wind and the blue line is of the with-wind model. The black triangle is the starting point of the ray tracing. The black circle at (12.5°S, 48.0°W) indicates where the wave was reflected.

295

Conclusion

We observed a gravity wave signature at the OH emission height (~ 87 km) and OI 630 nm emission height (< 240 km), those showed the same wave characteristic. Although the two waves look to be similar, the wave observed in the ionosphere might be a secondary wave. However, a direct influence of the primary wave in the OI 630 nm emission layer at around 200 km

300   altitude cannot be ruled out. We also observed fast concentric waves by the dTEC maps, which might be a secondary wave generated by a primary wave dissipated in the lower thermosphere. Both slow- and high-speed waves have their origin from a

convective spot in the ITCZ region. This is the first time to report the direct evidence of GW propagation from the troposphere to the ionosphere by optical imaging and dTEC measurements in the south American region.

Data availability

GNSS ground-based receiver data, airglow image data, and ionosonde data used in the present study are available at the EMBRACE data center website (http://www2.inpe.br/climaespacial/portal/ en/#). The satellite infrared thermal images (Figure 7) are obtained from the Geostationary Operational Environmental Satellite System 16 (GOES 16) data (http://satelite.cptec.inpe.br/home/ index.jsp), provided by the Center for Weather Forecasting and Climate Studies (CPTEC) in Brazil. Two atmospheric models were used in computing the gravity wave ray tracing (Figure 6): one is the MSIS-E-00 Atmospheric Model: https://ccmc.gsfc.nasa.gov/modelweb/models/msis_vitmo.php and the other is the empirical Horizontal Wind Model (HWM14) (Drob et al., 2015).

Acknowledgements

The present work was supported by CNPq (Conselho Nacional de Pesquisa e desenvolvimento) under the grants 310927/2020-0, 150569/2017-3, 161894/2015-1, 303511/2016, 300322/2022-4 and 306063/2020-4; Fundação de Amparo à Pesquisa do Estado de São Paulo (FAPESP) under the grant 2018/09066-8 and 2019/22548-4; and Coordenação de Aperfeiçoamento de Pessoal de Nível Superior (CAPES) under the process BEX4488/14-8. Paulino thanks to Fundação de Amparo à Pesquisa do Estado da Paraíba for the grants Demanda Universal Edital 09/20221 and Edital PRONEX termo de concessão 002/2019.

References

Azeem, I., Yue J., Hoffmann, L., Miller, S. D., Straka, W. C., and Crowley, G.: Multisensor profiling of a concentric gravity wave event propagating from the troposphere to the ionosphere, Geophys. Res. Lett., 42, 7874–7880, doi:10.1002/ 2015GL065903, 2015.

Bossert, K., Kruse, C. G., Heale, C. J., Fritts, D. C., Williams, B. P., Snively, J. B., Pautet, P.-D., and Taylor, M. J.: Secondary gravity wave generation over New Zealand during the DEEPWAVE campaign, J. Geophys. Res. Atmos., 122, 7834–7850, doi:10.1002/ 2016JD026079, 2017.

Chiang, C-Y., Tam, S. W-Y, and Chang, T-F.,: Variations of the 630.0 nm airglow emission with meridional neutral wind and neutral temperature around midnight, Ann. Geophys., 36, 1471–1481, https://doi.org/10.5194/angeo-36-1471-2018, 2018.

Colerico, M., Mendillo, M., Nottingham, D., Baumgardner, J., Meriwether, J., Mirick, J., Reinisch, B., Scali, J., Fesen, C., and Biondi, M.: Coordinated measurements of F region dynamics related to the thermospheric midnight temperature maximum, J. Geophys. Res.-Space, 101, 26783–26793, 1996.

330 Dare-Idowu, O., Paulino, I., Figueiredo, C. A. O. B., Medeiros, A. F., Buriti, R. A., Paulino, A. R., and Wrasse, C. M.: Investigation of sources of gravity waves observed in the Brazilian equatorial region on 8 April 2005, Ann. Geophys., 38, 507–516, https://doi.org/10.5194/angeo-38-507-2020, 2020.

Drob, D. P., Emmert, J. T., Meriwether, J. W., Makela, J. J., Doornbos, E., Conde, M., Hernandez, G., Noto, J., Zawdie, K. A., McDonald, S. E., et al.: An update to the Horizontal Wind Model (HWM): The quiet time thermosphere, Earth and Space
335 Science, 2, 301– 319, doi:10.1002/2014EA000089, 2015.

Essien, P., Paulino, I., Wrasse, C. M., Campos, J. A. V., Paulino, A. R., Medeiros, A. F., Buriti, R. A., Takahashi, H., Agyei-Yeboah, E., and Lins, A. N.: Seasonal characteristics of small- and medium-scale gravity waves in the mesosphere and lower thermosphere over the Brazilian equatorial region, Ann. Geophys., 36, 899–914, https://doi.org/10.5194/angeo-36-899-2018, 2018.

340 Essien, P., Figueiredo, C.A.O.B., Takahashi, H., Wrasse, C.M., Barros, D., Klutse, N.A.B., Lomotey, S.O., Ayorinde, T.T., Gobbi, D., Bilibio, A.V.: Long-Term Study on

Medium-Scale Traveling Ionospheric Disturbances Observed over the South American Equatorial Region, Atmosphere 2021, 12, 1409, https://doi.org/10.3390/atmos12111409, 2021.

Figueiredo, C. A. O. B., Buriti, R. A., Paulino, I., Meriwether, J. W., Makela, J. J., Batista, I. S., Barros, D., and Medeiros, A.
345 F.: Effects of the midnight temperature maximum observed in the thermosphere–ionosphere over the northeast of Brazil, Ann. Geophys., 35, 953–963, https://doi.org/10.5194/angeo-35-953-2017, 2017.

Figueiredo, C. A. O. B., Takahashi, H., Wrasse, C. M., Otsuka, Y., Shiokawa, K., & Barros, D.: Medium-scale traveling ionospheric disturbances observed by detrended total electron content maps over Brazil. J. Geophys. Res., Space Physics, 123, 2215–2227. https://doi.org/10.1002/ 2017JA025021, 2018.

350 Fritts, D. C., Vadas, S. L., Riggin, D. M., Abdu, M. A., Batista, I. S., Takahashi, H., Medeiros, A., Kamalabadi, F., Liu, H.-L., Fejer, B. G., and Taylor, M. J.: Gravity wave and tidal influences on equatorial spread F based on observations during the Spread F Experiment (SpreadFEx), Ann. Geophys., 26, 3235–3252, 2008, www.ann-geophys.net/26/3235/2008/, 2008.

Gong, Y., Zhou, Q., Zhang, S., Aponte, N., Sulzer, M., and Gonzalez S.: Midnight ionosphere collapse at Arecibo and its relationship to the neutral wind, electric field, and ambipolar diffusion, J. Geophys. Res.,117, A08332,
355 doi:10.1029/2012JA017530, 2012.

Hines, C. O.: Internal atmospheric gravity waves at ionospheric heights, Can. J. Phys., 38, 1441. https://doi.org/10.1139/p60-150, 1960.

Hocke, K., and Schlegel, K.: A review of atmospheric gravity waves and traveling ionospheric disturbances: 1982–1995, Ann. Geophys., 14, 917– 940, https://doi.org/10.1007/s00585-996-0917-6, 1996.

360   Kubota, M., Shiokawa, K., Ejiri, M.K. et al. Traveling ionospheric disturbances observed in the OI 630-nm nightglow images over Japan by using a multipoint imager network during the FRONT campaign. Geo. Phys. Res. Letts. 27(24), 4037–4040, DOI: 10.1029/2000GL011858, 2000.

Nicolls, M. J., Vadas, S. L., Aponte, N., and Sulzer, M. P.: Horizontal wave parameters of daytime thermospheric gravity waves and E-Region neutral winds over Puerto Rico. Journal of Geophysical Research: Atmospheres, 119, 576–600.

365   https://doi.org/10.1002/2013JA018988, 2014.

Nishioka, M., Tsugawa, T., Kubota, M., and Ishii, M.: Concentric waves and short-period oscillations observed in the ionosphere after the 2013 Moore EF5 tornado, Geophys. Res. Lett., 40, 5581–5586, doi:10.1002/2013GL057963, 2013.

Nyassor, P. K., Wrasse, C. M., Gobbi, D., Paulino, I., Vadas, S. L., Naccarato, K. P., et al. (2021). Case studies on concentric gravity waves source using lightning flash rate, brightness temperature and backward ray tracing at São Martinho da Serra

370   (29.44°S, 53.82°W). Journal of Geophysical Research: Atmospheres, 126, e2020JD034527. https://doi.org/10.1029/2020JD034527.

Picone, J. M., Hedin, A. E., Drob, D. P., and Aikin, A. C.: NRLMSISE-00 empirical model of the atmosphere: Statistical comparisons and scientific issues. Journal of Geophysical Research, 107(A12), 1468. https://doi.org/10.1029/2002JA009430, 2002.

375   Otsuka, Y.: Review of the generation mechanisms of post-midnight irregularities in the equatorial and low-latitude ionosphere. *Progress in Earth and Planetary Science*, *5*(1), 57. https://doi.org/10.1186/s40645-018-0212-7, 2008.

Paulino, I., Takahashi, H., Vadas, S. L., Wrasse, C. M., Sobral, J. H. A., Medeiros, A. F., et al.: Forward ray-tracing for medium scale gravity waves observed during the COPEX campaign, J. Atmos. Solar-Terr. Phys., 90-91(2012), 117–123. https://doi.org/10.1016/j.jastp.2012.08.006, 2012.

380   Ramkumar, T.K., Malik, M.A., Ganaie, B.A. et al. Airglow-imager based observation of possible influences of subtropical mesospheric gravity waves on F-region ionosphere over Jammu & Kashmir, India. Sci Rep 11, 10168 (2021). https://doi.org/10.1038/s41598-021-89694-3.

Smith, S. M., Vadas, S. L., Baggaley, W. J., Hernandez, G., and Baumgardner, J.: Gravity wave coupling between the mesosphere and thermosphere over New Zealand, J. Geophys. Res., Space Phys. 118, 2694-2707, doi:10.1002/jgra.50263,

385   2013.

Rottger, J.: Wave-like structures of large-scale equatorial spread-F irregularities, J. Atmos. Terr. Physics, 35,1195-1203, 1973

Takahashi, H., Batista, P.P., Buriti, R.A., Gobbi, D., Nakamura, T., Tsuda, T. and Fukao, S.: Response of the airglow OH emission, temperature and mesopause wind to the atmospheric wave propagation over Shigaraki, Japan, Earth Planet Sci., 51, 863–875, https://doi.org/10.1186/BF03353245, 1999.

390   Takahashi, H., Wrasse, C. M., Denardini, C. M., Pádua, M. B., de Paula, E.R., Costa, S.M.A., Otsuka, Y., Shiokawa, K., Monico, J.F.G., Ivo, A., Sant'Anna, N.: Ionospheric TEC weather map over South America. Space Weather 14:937–949. https://doi. org/10.1002/2016SW001474, 2016.

Takahashi, H., Wrasse, C. M., Figueiredo, C. A. O. B., Barros, D., Paulino, I., Essien, P., et al.: Equatorial plasma bubble occurrence under propagation of MSTID and MLT gravity waves. J. Geophys. Res.: Space Physics, 125, e2019JA027566.
395   https://doi.org/ 10.1029/2019JA027566, 2020.

Taori, A., Jayaraman, A. & Kamalakar, V. Imaging of mesosphere–thermosphere airglow emissions over Gadanki (13.51N, 79.21E). J. Atmos. Solar-Terrestrial Phys. 93, 21–28. https://doi.org/10.1016/j.jastp.2012.11.007 (2013).

Taylor, M. J., Pautet, P.-D., Medeiros, A. F., Buriti, R., Fechine, J., Fritts, D. C., Vadas, S. L., Takahashi, H., and São Sabbas, F. T.: Characteristics of mesospheric gravity waves near the magnetic equator, Brazil, during the SpreadFEx campaign, Ann.
400   Geophys., 27, 461–472, https://doi.org/10.5194/angeo-27-461-2009, 2009.

Tsuda, T.: Characteristics of atmospheric gravity waves observed using the MU (Middle and Upper atmosphere) radar and GPS (Global Positioning System) radio occultation, Proc Jpn Acad Ser B Phys Biol Sci. 2014 Jan 10; 90(1): 12–27. doi: 10.2183/pjab.90.12, 2014.

Vadas, S. L., and Liu, H.-L.: Numerical modeling of the large-scale neutral and plasma responses to the bodyforces created by
405   the dissipation of gravity waves from 6 h of deep convection in Brazil, J. Geophys. Res. Space Physics,118,2593–2617, doi:10.1002/jgra.50249, 2013.

Vadas, S. L., and Becker, E.: Numerical modeling of the excitation, propagation, and dissipation of primary and secondary gravity waves during wintertime at McMurdo Station in the Antarctic. J. Geophys. Res., Atmospheres, 123, 9326–9369. https://doi.org/10.1029/2017JD027974, 2018.

410   Vadas, S. L., and Crowley, G.: Sources of the traveling ionospheric disturbances observed by the ionospheric TIDDBIT sounder near Wallops Island on 30 October 2007, J. Geophys. Res., 115, A07324, doi:10.1029/2009JA015053, 2010.

Vadas, S. L.: Horizontal and vertical propagation and dissipation of gravity waves in the thermosphere from lower atmospheric and thermospheric sources, J. Geophys. Res., 112, A06305, doi:10.1029/2006JA011845, 2007.

Vadas, S. L., Xu, S., Yue, J., Bossert, K., Becker, E., and Baumgarten, G.: Characteristics of the quiet-time hot spot gravity
415   waves observed by GOCE over the Southern Andes on 5 July 2010, J. Geophys. Res., Space Physics, 124, 7034–7061, doi: 10.1029/2019JA026693, 2019.

Vadas, S. L. and Azeem, I.: Concentric secondary gravity waves in the thermosphere and ionosphere over the continental United States on March 25–26, 2015 from deep Convection. J. Geophys. Res., Space Physics, 126, e2020JA028275. https:// doi.org/10.1029/2020JA028275, 2021.

420   Wrasse, C. M, Takahashi, H., Medeiros, A. F., Lima, L. M., Taylor, M. J, Gobbi, D., and Fechine, J.: Determinação dos parâmetros de ondas de gravidade através da análise espectral de imagens de aeroluminescência. Revista Brasileira de Geofísica, 25(3), 257–265. https://doi.org/10.1590/S0102-261X2007000300003, 2007.

Wrasse, C. M., Figueiredo, C. A. O. B., Barros, D., Takahashi, H., Carrasco, A. J., Vital, L. F. R., Rezende, L. C. A., Egito, F., Rosa, G. M., and Sampaio, A. H. R.: Interaction between Equatorial Plasma Bubbles and a Medium-Scale Traveling

425   Ionospheric Disturbance, observed by OI 630 nm airglow imaging at Bom Jesus de Lapa, Brazil, Earth Planet. Phys., 5(5), 1–10. http://doi.org/10.26464/epp2021045, 2021.

Xu, X., Yu, D. and Luo, J.: Seasonal variations of global stratospheric gravity wave activity revealed by COSMIC RO data, 2017 Forum on Cooperative Positioning and Service (CPGPS), pp. 85-89, doi: 10.1109/CPGPS.2017.8075102, 2017.

430 Table Caption

Table 1. *Wave Characteristics obtained by the OH images in the MLT region (GW-1 and GW-2), and OI 630 nm images in the thermosphere (MSTID-1)* ~~and dTEC maps in the ionosphere (MSTID-2).~~ *(The values in parentheses are the error range.)*

435 Figure Captions

Fig. 1. Geographically coordinated OH images observed at Bom Jesus da Lapa (BJL), 13.3°S, 43.5°W, geomag.14.1°S, at 23:30 UT (left), 23:41 UT (center) and 23:51 UT (right) on the night of 18-19 January 2020. Blue dots indicate the zenith of BJL. The blue arrows indicate the wave fronts of the longer wavelength one (GW-2). The red-arrow indicates the direction of propagation.

440 *Fig. 2. Keograms of OH images observed at BJL in the night of 18-19 January 2020. Meridian cuts along the W-E direction (upper panel) and the S-N direction (lower panel) are shown as a function of time from 22:00 to 30:00 (06:00) UT. The red color rectangular boxes are where the FFT spectral analysis were taken.*

Fig. 3. Geographically coordinated OI 630 nm images observed at Bom Jesus da Lapa (BJL) at 03:20 UT (left), 03:34 UT(center) and 03:48 UT (right) on the night of 18-19 January 2020. The top 3 images are original and the
445 *bottom 3 images are residual subtracted from the one hour averaged image. Blue dots indicate the location of BJL. MSTID-1 (lower/middle), EPBs (upper left corner) and MTM (upper left) can be seen (see Text).*

~~*Fig. 4 dTEC Map in the equatorial and low latitude of Brazil, taken at 03:44 UT (00:44 LT at 45°W), 18-19 January 2020. The black line indicates the geomagnetic equator, and the blue circumferences indicate wave crests of the MSTID. The top/left corner "0.25(5x5)" indicates a spatial resolution of the map as 1.25° x 1.25° (~130 x 130 km).*~~

450 ~~*Fig. 5. Keograms of dTEC: the longitudinal cut at 13.0°S (top) and the latitudinal cut at 43.0°W (bottom) as a function of Time (UT). The rectangular boxes highlight where the FFT spectral analysis was applied.*~~

Fig. 6. Ray tracing (backward and forward) of the observed gravity wave (λ_h=217.9 km) starting at 87 km altitude at BJL on the night of 18 January 2020 at 23:00 UT. The vertical trajectory versus time (top) and horizontal distance (bottom) are shown. The red line is of the case of no-wind and the blue line is of the with-wind model. The

455 *blue triangle is the starting point of the ray tracing. The background map is the cloud top temperature from NOAA GOES 16 meteorological satellite data (10.35 μ) on 18 January 2020 at 19:00 UT.*

Fig. 7. Backward Ray-Tracing of the MSTID circular waves, starting from 300 km altitude at (17.0 °S, 43.0 °W) at 03:40 UT. The vertical trajectory versus time (top) and horizontal distance (bottom) are shown. The red line is in the case of the no-wind and the blue line is of the with-wind model. The black triangle is the starting point of the ray tracing. The black circle at (12.5 °S, 48.0 °W) indicates where the wave was reflected.

460